Application of the Fourier pseudospectral time-domain method in orthogonal curvilinear coordinates for near-rigid moderately curved surfaces

Maarten HornikxDidier DragnaVEO

Application of the Fourier pseudospectral time-domain method in orthogonal curvilinear coordinates for near-rigid moderately curved surfaces

Maarten Hornikx[a)]
Building Physics and Services, Department of the Built Environment, Eindhoven University of Technology, P.O. Box 513, 5600 MB Eindhoven, The Netherlands

Didier Dragna
Laboratoire de Mécanique des Fluides et d'Acoustique, UMR CNRS 5509, École Centrale de Lyon, Université de Lyon, 36 Avenue Guy de Collongue, 69134 Écully Cedex, France

The Fourier pseudospectral time-domain method is an efficient wave-based method to model sound propagation in inhomogeneous media. One of the limitations of the method for atmospheric sound propagation purposes is its restriction to a Cartesian grid, confining it to staircase-like geometries. A transform from the physical coordinate system to the curvilinear coordinate system has been applied to solve more arbitrary geometries. For applicability of this method near the boundaries, the acoustic velocity variables are solved for their curvilinear components. The performance of the curvilinear Fourier pseudospectral method is investigated in free field and for outdoor sound propagation over an impedance strip for various types of shapes. Accuracy is shown to be related to the maximum grid stretching ratio and deformation of the boundary shape and computational efficiency is reduced relative to the smallest grid cell in the physical domain. The applicability of the curvilinear Fourier pseudospectral time-domain method is demonstrated by investigating the effect of sound propagation over a hill in a nocturnal boundary layer. With the proposed method, accurate and efficient results for sound propagation over smoothly varying ground surfaces with high impedances can be obtained. © 2015 Acoustical Society of America.
[http://dx.doi.org/10.1121/1.4922954]

[VEO]   Pages: 425–435

I. INTRODUCTION

Partly driven by the advances in computer power, wave-based modeling for atmospheric sound propagation purposes has attracted increased attention in recent years. Wave-based modeling is especially of interest for treating problems including effects of the ground surface, obstacles, and meteorology. Some recently reported methods are the finite-difference time-domain method (FDTD),[1] the three dimensional parabolic equation (PE) method,[2] and the transmission line model (TLM).[3] Another time-domain method is the Fourier pseudospectral time-domain method (PSTD).[4,6] PSTD is an attractive full volume-discretization method as only two spatial points are required to resolve a wavelength at spectral accuracy. It enables to solve the linearized Euler equations (LEE), and effects as reflection, diffraction and meteorological conditions are accurately accounted for.[4,5] A limitation in PSTD is the modeling of boundary conditions, but treatment of rigid boundaries and boundaries with a different density have successfully been presented in Ref. 4. Also, a local grid refinement technique has been proposed.[5] The current PSTD method can only accurately solve staircase-type geometries. For non-staircase-type geometries that occur in real-life, e.g., oblique or curved surfaces, the

method is only approximate. The error related to staircase-type modeling of non-staircase-type boundaries is similar as in FDTD methods, when the same discretization is used, and has been reported before in Ref. 7. In related numerical methodologies to the Fourier PSTD method, i.e., the Chebyshev PSTD method and the FDTD method, a transform of the coordinate system has been employed in order to relax the constraints imposed by the Cartesian grid. An often-used approach is the curvilinear coordinate transform,[8–10] and also other approaches to model non-staircase boundaries in FDTD have recently been presented in Refs. 11 and 12. Although application of the curvilinear coordinate transform for the Fourier PSTD method has appeared in earlier work by Nielsen,[13] and in recent work by Albin *et al.* in combination with the Fourier continuation PSTD method,[6] the combination with appropriate boundary conditions has not been encountered. Here, a curvilinear transformation is therefore applied to the extended Fourier PSTD method as presented in Ref. 4 with the purpose to obtain an efficient and accurate wave-based method for atmospheric sound propagation with frequency independent real-valued impedance boundary conditions. It needs to be stressed that the current work should be considered as an intermediate step towards a method with frequency-dependent impedance boundary conditions.

The used methodology to solve atmospheric sound propagation in the presence of non-staircase surfaces is presented

---

[a)]Electronic mail: m.c.j.hornikx@tue.nl

in Sec. II. The governing equations are described, as well as the curvilinear transform approach as adopted in this work, including the algorithm used to map an arbitrary geometry onto a Cartesian grid in a rectangular domain. The Fourier PSTD method, the numerical methodology to solve the equations, is also described. In Sec. III, the geometrical configurations as studied in this work are presented, as well as the used boundary and initial conditions of the computations. Results are presented in Sec. IV.

The performance of the Fourier PSTD method to solve the curvilinear acoustic equations is first investigated in free field. Then, the accuracy of treating a boundary with various impedance properties is addressed, as well as propagation over a trapezoidal and Gaussian shaped profile. Finally, the ability of the method to model outdoor sound propagation over a hill in a nocturnal boundary layer is demonstrated.

II. METHODOLOGY

A. Curvilinear transformed linearized Euler equations

Atmospheric sound propagation can be described by the LEE. For outdoor applications with sound propagating mostly horizontally, the effective sound speed approach is often a good assumption to include effects of moving media as well as a spatially-dependent temperature, e.g., Ref. 14. It needs to be stressed however that this is a simplification not correctly handling meteorological effects for all configurations. For dry air, the effective sound speed can be computed as

$$c_{\text{eff}} = \sqrt{\gamma R [273.15 + T(\mathbf{r})]/M} + \mathbf{u}_{0,x}(\mathbf{r}), \qquad (1)$$

where $\mathbf{r} = (x, z)$ is the coordinate vector in two dimensions, $\gamma = 1.4$ the specific heat ratio for air, $R = 8.3145$ J/mol K the molar gas constant, $M = 0.0290$ kg/mol the mean molar mass of air, T the temperature in °C, $\mathbf{u}_{0,x}$ the mean velocity of the medium in x-direction.

With the effective sound speed approach, the linearized Euler equations in a two dimensional (2D) coordinate system read

$$\begin{aligned}
\frac{\partial p}{\partial t} &= -\rho c_{\text{eff}}^2 \left(\frac{\partial u_x}{\partial x} + \frac{\partial u_z}{\partial z} \right), \\
\frac{\partial u_x}{\partial t} &= -\frac{1}{\rho} \frac{\partial p}{\partial x}, \\
\frac{\partial u_z}{\partial t} &= -\frac{1}{\rho} \frac{\partial p}{\partial z},
\end{aligned} \qquad (2)$$

with the acoustic velocity $\mathbf{u} = (u_x, u_z)$ and the acoustic pressure p, and where the medium density ρ is allowed to vary throughout the domain. In this work, air absorption has been neglected and we have used $\rho = 1.2$ kg/m^3 and $c_{\text{eff}} = 340$ m/s for homogeneous medium configurations. The acoustic problem is described by Eq. (2), completed by boundary and initial conditions. A popular way to solve such a problem is by meshing the whole domain by a Cartesian mesh and to approximate the solution at every mesh point through numerically solving Eq. (2) by FDTD or PSTD methods. However, the Cartesian mesh as used in these methods will not capture arbitrarily shaped

boundaries, i.e., non-staircase-type boundaries, in an accurate way without having to over resolve the mesh. To be able to use a solution method as FDTD and PSTD with a Cartesian mesh for problems with non-staircase-type boundaries, a coordinate transform is applied from the physical domain (an arbitrary shape and with coordinates x,z) to the curvilinear domain (a rectangular shape with coordinates ξ, η). The curvilinear coordinates can thus be expressed as a function of the physical coordinates, i.e., $\xi = \xi(x, z)$ and $\eta = \eta(x, z)$. Using a chain-rule expansion, the relations Eq. (2) then read

$$\begin{aligned}
\frac{\partial p}{\partial t} &= -\rho c_{\text{eff}}^2 \left[\left(\xi_x \frac{\partial}{\partial \xi} + \eta_x \frac{\partial}{\partial \eta} \right) u_x + \left(\xi_z \frac{\partial}{\partial \xi} + \eta_z \frac{\partial}{\partial \eta} \right) u_z \right], \\
\frac{\partial u_x}{\partial t} &= -\frac{1}{\rho} \left(\xi_x \frac{\partial}{\partial \xi} + \eta_x \frac{\partial}{\partial \eta} \right) p, \\
\frac{\partial u_z}{\partial t} &= -\frac{1}{\rho} \left(\xi_z \frac{\partial}{\partial \xi} + \eta_z \frac{\partial}{\partial \eta} \right) p,
\end{aligned} \qquad (3)$$

where the notation $i_j = \partial i / \partial j$ is employed to express the partial derivatives of the coordinate functions. Note that the Chebyshev PSTD method is a special case of a transform of the curvilinear Fourier PSTD method, with $\xi = \arccos(x)$ and $\eta = \arccos(z)$, with $-1 \leq x, z \leq 1$.

B. Fourier PSTD method

The numerical method adopted here to solve Eq. (2) in the curvilinear coordinate system is the Fourier PSTD method. The interested reader is referred to Ref. 4 for a more rigorous presentation of the method. In PSTD, the geometries of interest are discretized by an equidistant Cartesian mesh with spatially staggered pressure and velocity nodes. The equations are marched in time by a low-storage optimized six-stage Runge-Kutta method.[15] At every discrete time step, the spatial derivatives are computed using the Fourier pseudospectral method. For evaluation of the ξ-derivative of pressure and a velocity u_ξ along an unbounded ξ-direction with dimension $M\Delta\xi$, the following expressions are used:

$$\begin{aligned}
\frac{\partial p(n\Delta\xi^+)}{\partial \xi} &= \mathcal{F}_\xi^{-1} \left\{ j k_\xi e^{-j k_\xi (\Delta\xi/2)} \mathcal{F}_\xi [p(m\Delta\xi)] \right\}, \\
\frac{\partial u_\xi(n\Delta\xi)}{\partial \xi} &= \mathcal{F}_\xi^{-1} \left\{ j k_\xi e^{j k_\xi (\Delta\xi/2)} \mathcal{F}_\xi [u_\xi(m\Delta\xi^+)] \right\},
\end{aligned} \qquad (4)$$

where $m\Delta\xi^+$ denotes $m\Delta\xi + (\Delta\xi/2)$, $\mathcal{F}_\xi$ is the forward and $\mathcal{F}_\xi^{-1}$ the inverse discrete Fourier transform over and to the ξ-variable, and $0 \leq n, m \leq M$. The spatial derivatives are multiplied in the wave number domain by $e^{\pm j k_\xi (\Delta\xi/2)}$ to evaluate the derivatives at positions staggered by $\mp(\Delta\xi/2)$. Since fast Fourier transforms (FFTs) are used to calculate derivatives, only two spatial points per (projected) wavelength are needed with this method. To account for reflecting boundaries, derivatives along directions with a boundary medium with a different density from air are used, as presented in Refs. 4 and 16. According to these references, for the ξ-derivative of pressure and velocity component u_ξ along ξ-direction with a boundary interface at $\xi = 0$ and dimension $-M_1\Delta\xi < \xi < M_2\Delta\xi$, the following expressions are obtained

Maarten Hornikx and Didier Dragna

$$\frac{\partial p(n\Delta\xi^+)}{\partial\xi} = \mathcal{F}_\xi^{-1}\left(jk_\xi e^{-jk_\xi(\Delta\xi/2)}\mathcal{F}_\xi\begin{bmatrix}p_1\\p_2\end{bmatrix}\right), \qquad \begin{aligned}&-M_1 \leq n \leq -1,\\&0 \leq n \leq M_2 - 1,\end{aligned}$$

$$\frac{\partial u_\xi(n\Delta\xi)}{\partial\xi} = \mathcal{F}_\xi^{-1}\left(jk_\xi e^{jk_\xi(\Delta\xi/2)}\mathcal{F}_\xi\begin{bmatrix}u_{\xi,1}\\u_{\xi,2}\end{bmatrix}\right), \qquad \begin{aligned}&-M_1 \leq n \leq -1,\\&0 \leq n \leq M_2 - 1.\end{aligned} \tag{5}$$

For the derivatives of the pressure and normal velocity component in medium 1, i.e., $\xi \leq 0$, the following is used

$$p_1(m\Delta\xi) = \begin{cases} p(m\Delta\xi), & -M_1 \leq m \leq -1,\\ R_{1,1}p(-m\Delta\xi) + T_{2,1}p(m\Delta\xi), & 0 \leq m \leq M_2 - 1, \end{cases}$$

$$u_{\xi,1}(m\Delta\xi) = \begin{cases} u_\xi(m\Delta\xi^+), & -M_1 \leq m \leq -1,\\ -R_{1,1}u_\xi(-m\Delta\xi^+) + T_{1,2}u_\xi(m\Delta\xi^+) & 0 \leq m \leq M_2 - 1. \end{cases}$$

Note that for p_1 and $u_{\xi,1}$, derivatives are computed for $-M_1\Delta\xi \leq \xi < M_2\Delta\xi$, but are only physically valid and used for $\xi \leq 0$. For the derivatives in medium 2, i.e., $\xi \geq 0$, the following is used

$$p_2(m\Delta\xi) = \begin{cases} R_{2,2}p(-m\Delta\xi) + T_{1,2}p(m\Delta\xi), & -M_1 \leq m \leq -1,\\ p(m\Delta\xi), & 0 \leq m \leq M_2 - 1, \end{cases}$$

$$u_{\xi,2}(m\Delta\xi) = \begin{cases} -R_{2,2}u_\xi(-m\Delta\xi^+) + T_{2,1}u_\xi(m\Delta\xi^+), & -M_1 \leq m \leq -1,\\ u_\xi(m\Delta\xi^+), & 0 \leq m \leq M_2 - 1. \end{cases}$$

Here, $R_{j,j}$ and $T_{j,l}$ are the physical reflection and transmission factors from medium j to medium j or l. In this work, the transform of (x, z), the coordinates of the physical domain, to (ξ, η), the coordinates of the curvilinear domain, is obtained using a Schwarz-Christoffel (SC) transform, utilizing the SC toolbox.[17,18] A second transform is then made to transform the curvilinear domain (a rectangle) that arises from the SC transform into a rectangle for which an equidistant mesh can be generated. A major interest of the SC transform is that it preserves, from the physical to the curvilinear domain, the grid angles between the grid lines. In particular, it allows us to obtain an orthogonal grid. However, stretching of the physical grid relative to the curvilinear grid [see, e.g., Fig. 1(a)] causes enlarged grid spacing in the physical
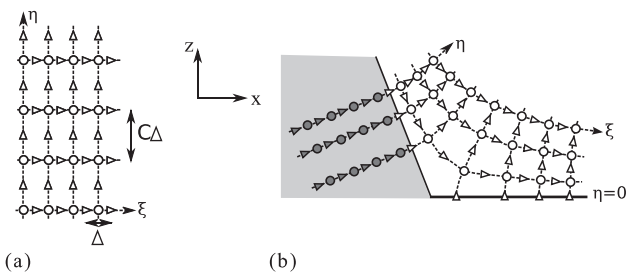

FIG. 1. Excerpt of computational grid with staggered positions of pressure (circles) and velocity components (triangles) (a) for configuration (A) and (b) for configuration (B4) near the trapezoid, see Fig. 2. Gray-colored positions indicate the locations of the grid in the locally reacting medium, in which derivatives are only computed perpendicular to the medium interface.

coordinate system. The consequence is a lower maximum resolved frequency, which will be reported in Sec. IV.

The relations of Eq. (5) to compute the velocity component normal to the boundary will only be approximate for the computation of the ξ-derivative of the u_x and u_z components, as they are generally not perpendicular to the ξ-direction. This will be a limitation when solving Eq. (3) by the Fourier PSTD methodology. To overcome this issue, the velocity components u_ξ and u_η of the curvilinear coordinate system are computed instead of the velocity components u_x and u_z of the physical coordinate system. For this purpose, u_ξ and u_η need to be expressed as a function of u_x and u_z. Two main bases are used to express the curvilinear components of a vector. In the first one, which is the covariant basis, the basis vectors are tangent to the curvilinear coordinates. In the second one, which is the contravariant basis, the basis vectors are orthogonal to the curvilinear coordinates. As the physical grid used in this work is orthogonal, these two approaches are identical. Denoting the unit vectors of the contravariant basis in the ξ and η directions by $\mathbf{e}^\xi = \nabla\xi/|\nabla\xi|$ and $\mathbf{e}^\eta = \nabla\eta/|\nabla\eta|$, with $\nabla\xi = (\xi_x, \xi_z)$ and $\nabla\eta = (\eta_x, \eta_z)$, the components of the acoustic velocity in the curvilinear coordinate system are given by

$$u_\xi = \mathbf{u} \cdot \mathbf{e}^\xi = \frac{\xi_x u_x + \xi_z u_z}{\sqrt{\xi_x^2 + \xi_z^2}},$$

$$u_\eta = \mathbf{u} \cdot \mathbf{e}^\eta = \frac{\eta_x u_x + \eta_z u_z}{\sqrt{\eta_x^2 + \eta_z^2}}. \tag{6}$$

In addition, the orthogonality of the curvilinear coordinate system leads to the relation $e^\xi \cdot e^\eta = 0$, which implies

$$\xi_x \eta_x + \xi_z \eta_z = 0. \tag{7}$$

Introducing Eq. (6) in Eq. (3) and using Eq. (7), we then find

$$\frac{\partial p}{\partial t} = -\rho c_{eff}^2 \left[\left(A_1 + A_2 \frac{\partial}{\partial \xi} \right) u_\xi + \left(B_1 + B_2 \frac{\partial}{\partial \eta} \right) u_\eta \right],$$
$$\frac{\partial u_\xi}{\partial t} = -\frac{1}{\rho} A_2 \frac{\partial p}{\partial \xi},$$
$$\frac{\partial u_\eta}{\partial t} = -\frac{1}{\rho} B_2 \frac{\partial p}{\partial \eta},$$

with

$$A_1 = -\frac{\nabla \xi \cdot (\nabla \eta)_\eta}{|\nabla \xi|} = -\frac{\xi_x(\eta_x)_\eta + \xi_z(\eta_z)_\eta}{\sqrt{\xi_x^2 + \xi_z^2}},$$

$$A_2 = |\nabla \xi| = \sqrt{\xi_x^2 + \xi_z^2},$$

$$B_1 = -\frac{\nabla \eta \cdot (\nabla \xi)_\xi}{|\nabla \eta|} = -\frac{\eta_x(\xi_x)_\xi + \eta_z(\xi_z)_\xi}{\sqrt{\eta_x^2 + \eta_z^2}},$$

$$B_2 = |\nabla \eta| = \sqrt{\eta_x^2 + \eta_z^2}. \tag{8}$$

The spatial derivatives of the acoustic variables in Eq. (8) are computed using Eq. (4) in free field and Eq. (5) in the presence of a boundary medium. The boundary medium is approached as being locally reacting by not computing derivatives in the boundary medium, parallel to the interface. This approach is approximative, as the Fourier PSTD method of Eq. (5) is strictly valid for extendedly reacting media with equal speeds of sound. Modelling an extendedly reacting boundary medium by the curvilinear Fourier PSTD method would imply that a separate conformal map of the boundary medium should be made. The location of the grid points at the media interfaces, i.e., the normal velocity components, would however be different at both sides of the interface. The local reaction approach is therefore adopted here [see Fig. 1(b)], and the following equations are solved in a boundary medium with the boundary parallel to the ξ-direction:

$$\frac{\partial p}{\partial t} = -\rho_{bd} c_{eff}^2 \frac{\partial u_\eta}{\partial \eta},$$
$$\frac{\partial u_\eta}{\partial t} = -\frac{1}{\rho_{bd}} \frac{\partial p}{\partial \eta}. \tag{9}$$

Subscript bd denotes the boundary medium and the sound speed c_{eff} for a homogeneous atmosphere is used. The first order spatial derivatives of the metric quantities ξ_x and η_z in Eq. (8) are directly obtained from numerical evaluations of the Schwarz-Christoffel mapping function. The cross derivatives ξ_z and η_x are obtained from using the Cauchy-Riemann equations. Second order spatial derivatives are computed by high order finite differences.

All these derivatives are computed once, prior to marching the acoustic variables in time. The metric quantities should respect the Geometric Conservations Laws (CGL), see Ref. 9. For the 2D case and the used non-conservative form of the equations, the approach followed is not expected to introduce large errors.

C. Non-reflecting boundaries and stability

Non-reflecting boundaries are obtained by imposing a perfectly matched layer (PML), either to the boundary media as well as to the outer boundaries of the air domain, and are used as proposed for the Fourier PSTD method in Ref. 4. This PML implies that the pressure is split into its components $p = p_\eta + p_\xi$. These relations are used when imposing initial conditions, as described in Sec. III. In this work, the following equations are used to include non-reflecting boundary conditions:

$$\frac{\partial p_\xi}{\partial t} = -\rho c_{eff}^2 \left[\left(A_1 + A_2 \frac{\partial}{\partial \xi} \right) u_\xi \right] - \sigma_\xi(\mathbf{r}) p_\xi,$$
$$\frac{\partial p_\eta}{\partial t} = -\rho c_{eff}^2 \left[\left(B_1 + B_2 \frac{\partial}{\partial \eta} \right) u_\eta \right] - \sigma_\eta(\mathbf{r}) p_\eta,$$
$$\frac{\partial u_\xi}{\partial t} = -\frac{1}{\rho} A_2 \frac{\partial p}{\partial \xi} - \sigma_\xi(\mathbf{r}) u_\xi,$$
$$\frac{\partial u_\eta}{\partial t} = -\frac{1}{\rho} B_2 \frac{\partial p}{\partial \eta} - \sigma_\eta(\mathbf{r}) u_\eta, \tag{10}$$

with the PML coefficients $\sigma(\mathbf{r}) = [\sigma_\xi(\mathbf{r}), \sigma_\eta(\mathbf{r})]^T$ being zero or positive in the PML and zero elsewhere, see Ref. 4 for their values. The equations are solved as in Ref. 4.

The stability of the Fourier PSTD method is determined by the stability criteria arising from the used Runge-Kutta method,[15] i.e., the discrete time step should obey the following condition:

$$\Delta t_{stab} < \frac{1}{0.8 f_{max}}, \tag{11}$$

with

$$f_{max} = \sqrt{D} \left(\frac{\Delta^c}{c_{eff}} \right)_{min}^{-1},$$

where f_{max} is an estimate of the maximum frequency related to the discretization using the Fourier pseudospectral method. Note that in 2D, this frequency is larger than the frequency up to which accurate results are expected. Further D is the dimensionality of the problem and $(\Delta^c/c_{eff})_{min}$ the minimal value of the ratio of the spatially dependent grid spacing in the physical grid Δ^c over the speed of sound. For a medium with a constant speed of sound, this implies

$$\left(\frac{\Delta^c}{c_{eff}} \right)_{min} = \left(\frac{\Delta_{min}^c}{c_{eff}} \right), \tag{12}$$

where $\Delta_{min}^c = \min(S_{\xi,min}, S_{\eta,min})\Delta$ is the smallest spatial discretization of the physical grid and $S_\xi = \sqrt{x_\xi^2 + z_\xi^2}$ and

$S_\eta = \sqrt{x_\eta^2 + z_\eta^2}$ are the stretching factors in ξ and η directions. This leads to

$$\Delta t_{\text{stab}} < \frac{1}{0.8\sqrt{D}} \left(\frac{\Delta^c}{c_{\text{eff}}} \right)_{\text{min}}. \tag{13}$$

The estimate of the frequency up to which accuracy results are expected is $f = \frac{1}{2}(\Delta^c/c_{\text{eff}})_{\text{max}}^{-1}$. It is important to note that the accuracy constraints originating from the Runge-Kutta method requires $\Delta t_{\text{acc}} < \frac{1}{2}(\Delta^c/c_{\text{eff}})_{\text{max}}$ for accurate results up to this frequency. A value of $\Delta t = \min(\Delta t_{\text{acc}}, \Delta t_{\text{stab}})$ has been used in this manuscript.

III. CONFIGURATIONS

To investigate the applicability of the curvilinear Fourier PSTD method, various configurations have been defined. The first configuration is a free field case. Figure 2(A) shows the source and receivers locations in free field. Receivers are located in an arc around the source at a distance of 20Δ. The second configuration is a sound source over an outdoor impedance surface or a rigid surface with an impedance strip, see Fig. 2(B). The impedance strip is either flat, or is shaped as a trapezoid or Gaussian shape according to the following functions:

$$z_{\text{Trap}} = \begin{cases} \dfrac{x + 6\Delta}{4\Delta} H & \text{for} \quad -6\Delta \le x \le -2\Delta \\ H & \text{for} \quad -2\Delta \le x \le 2\Delta \\ \dfrac{-x + 6\Delta}{4\Delta} H & \text{for} \quad 2\Delta \le x \le 6\Delta, \end{cases}$$

$$z_{\text{Gauss}} = H \frac{e^{-(1/2)(6x/w)^2} - e^{-(1/2)(3)^2}}{1 - e^{-(1/2)(3)^2}},$$

$$\text{for} - w/2 \le x \le w/2 \tag{14}$$

with H the height of the trapezoid or Gaussian shape, and w the width of the Gaussian shape.

The impedance strip has been assigned a real valued impedance of $Z = (\rho_{bd}/\rho) = -(R_n + 1)/(R_n - 1)$, with $R_n = \sqrt{1 - \alpha_n}$ the reflection factor for sound waves normal incident to the surface and α_n the absorption coefficient for
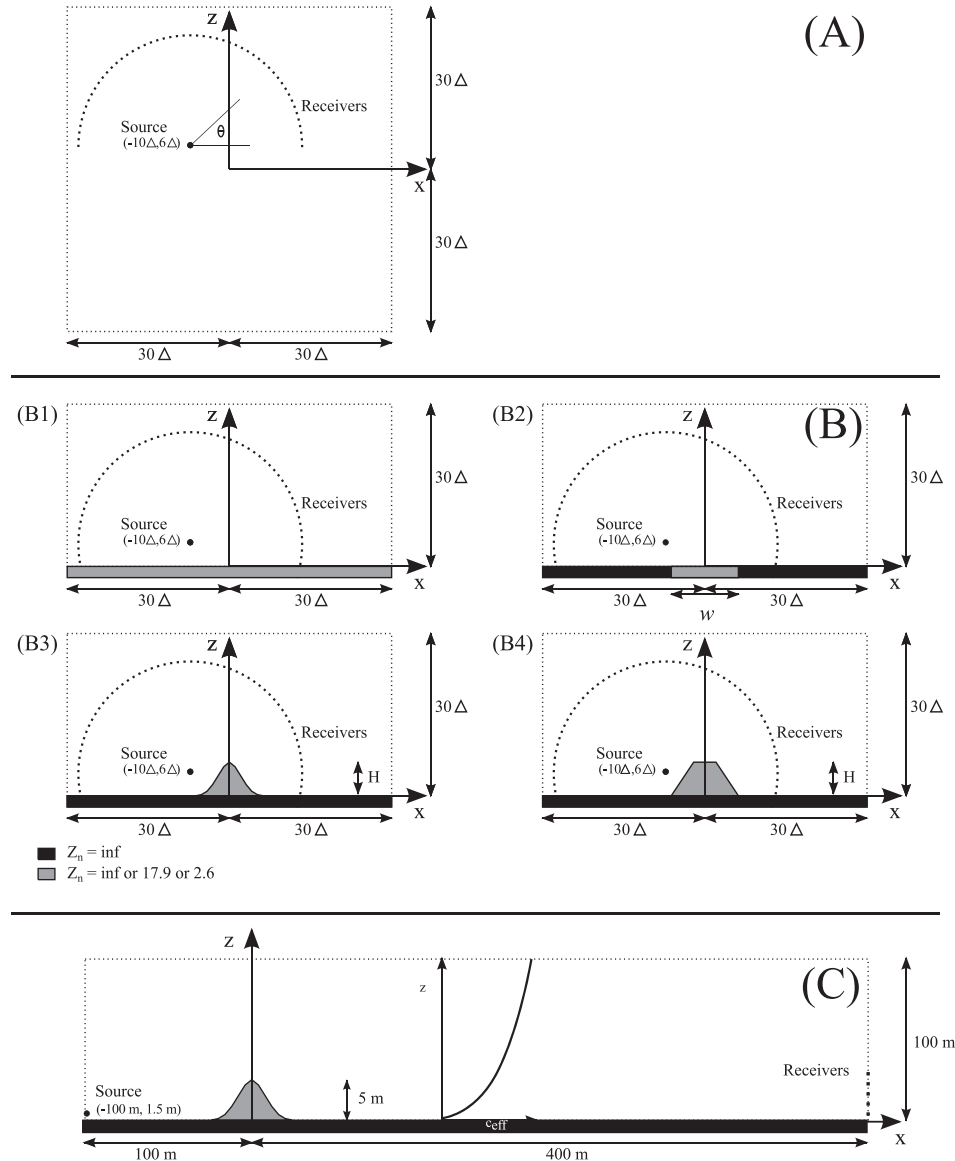

FIG. 2. Studied configurations. Dashed lines represent reflection free boundaries, which are surrounded by a 50 cell-wide PML layer. Non-rigid ground surfaces are 50 cells wide (including PML). (A) Free field, (B) ground surface: (B1) flat ground, (B2) flat ground with strip, (B3) Gaussian shaped strip, (B4) trapezoidal shaped strip, (C) ground surface with hill and effective sound speed profile according to a nocturnal boundary layer.

normal sound incidence. Three values have been used, $\alpha_n = 0$, $\alpha_n = 0.2$, and $\alpha_n = 0.8$. The source is located at coordinates $x = -10\Delta$, $z = 6\Delta$, and receivers are located around the source as in the free field configuration (A). Finally, configuration (C) is designed to demonstrate the applicability of the method, i.e., combining a non-staircase boundary with an inhomogeneous medium. The configuration includes a hill whose center is located at a horizontal distance of 100 m from the source position. The shape of the hill is described by z_{Gauss} in Eq. (14), with $w = 50$ m and $H = 5$ m. Sound propagation in a nocturnal boundary layer (NBL) is considered in Fig. 2(C), with temperature gradient (according to Ref. 14)

$$T = T_0 + \Delta T(1 - e^{-\alpha z'}) + \Gamma z', \tag{15}$$

with $T_0 = 14.4\,°C$, $\Delta T = 11.1\,°C$, $\alpha = 0.021\,m^{-1}$ and $\Gamma = 0.00975\,°C/m$. The quantity z' is here defined as the height above the ground surface. The effect of the hill on the meteorological conditions is not considered here. The wind profile is computed according to

$$u_{0,x}(z') = u_{h_2} \frac{\log(z'/h_1)}{\log(h_2/h_1)}, \tag{16}$$

with $u_{h2} = 3.3$ m/s, $h_2 = 3.4$ m, $h_1 = 0.1$ m and $u_{0,x}(z') = 0$ m for $z' < h_1$. The NBL is ill behaved and difficult to quantify. Typically, it is associated with low wind speeds near the surface as the air layer above has a thermal profile that is stratified.[19] The temperature and wind velocity effects are incorporated by using the effective sound speed approach [see Eq. (1)]. In all configurations, acoustic waves are excited by either prescribing a time-dependent pressure function at a certain location in the domain, or by imposing non-zero initial pressure conditions. For the investigation in configurations (A) and (C), a time-dependent pressure function is used at a specified grid point. In that case, the right side of the first two equations in Eq. (10) gets the source term $-s(t)\delta(\mathbf{r}|\mathbf{r}_s) = -s(t)\delta(\boldsymbol{\rho}|\boldsymbol{\rho}_s)/(S_\xi S_\eta)$, with $\boldsymbol{\rho}(\xi, \eta)$ the coordinate vector in curvilinear coordinates and $\mathbf{r}_s$ and $\boldsymbol{\rho}_s$ the position of the source in the physical and curvilinear domain, respectively. The time-dependent function $s(t)$ is given by

$$s(t) = A\sin(2\pi f_c t)e^{-a(t-t_c)^2}, \tag{17}$$

with $t_c = 27.2\Delta/c_0$ the center time of the source, $A = 1/D$, $f_c = c_0/(16\Delta)$ and $a = 3c_0^2/(64\Delta^2)$. The parameter c_0 is the reference sound speed set to 340 m/s. As the discrete position of the source does not necessarily coincide with a grid point for the other configurations, non-zero initial pressure conditions have been imposed for the configurations B,

$$
\begin{aligned}
p(\mathbf{r}, t = 0) &= e^{-\beta|r-r_s|^2}, \\
p_\xi(\mathbf{r}, t = 0) &= \cos^2(\theta)p(\mathbf{r}, t_0), \\
p_\eta(\mathbf{r}, t = 0) &= \sin^2(\theta)p(\mathbf{r}, t_0), \\
u_\xi(\mathbf{r}, t = 0) &= u_\eta(\mathbf{r}, t_0) = 0,
\end{aligned} \tag{18}
$$

with θ the angle from a grid point to the source in the physical domain, see Fig. 2(A), and $\beta = 3e^{-6}c_0^2/\Delta^2$.

IV. RESULTS

Results in this section are presented as a function of the number of grid points per wavelength $N_\lambda = c_0/(f\Delta)$. For this purpose, a discrete Fourier transform has been applied to the computed time dependent pressure signals at the receivers positions. Level differences have statistically been averaged over receiver positions and are computed as $\overline{\Delta L_p} = (1/N)\sum_{n=1}^{N} \Delta L_{p,n}$ with N the number of receiver positions, $\Delta L_{p,n} = |L_{p,n} - L_{p,ref}|$, with $L_{p,n}$ the computed result and $L_{p,ref}$ the reference result, which is different for the various configurations.

A. Free field

To study the effect of stretching and compression of the grid, the scale of the vertical dimension of the physical domain is varied, while the number of discrete grid points is kept equal, i.e., $S_\xi(x, z) = 1$ and $S_\eta(x, z) = C$, and C ranges from 1/8 to 8. Figure 3 shows the results of $\Delta L_{p,n}$, with $L_{p,ref}$ the computed level for $C = 1$. In Fig. 3(a) $\Delta L_{p,n}$ is displayed for $C = 4$. The error can be seen to appear for $N_\lambda \leq 8$. The error is largest in the z-direction, corresponding to a receiver angle $\theta = 90°$. In Fig. 3(b), $\overline{\Delta L_p}$ is plotted for the various values of C. The white circles in the plot correspond to the expected smallest resolved wavenumber, expressed
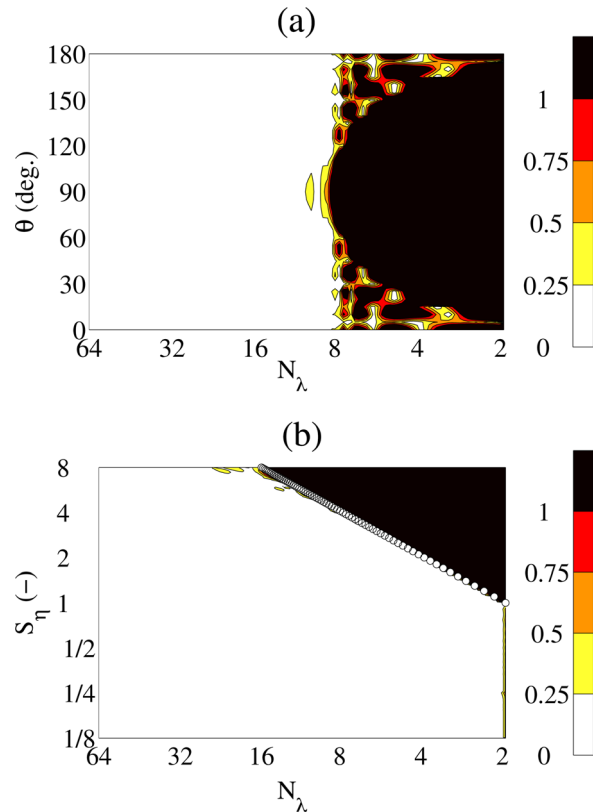

FIG. 3. (Color online) Results for configuration (A) with $S_\eta(x, z) = C$. (a) $\Delta L_{p,n}$ (dB) as a function of the receiver position and the grid resolution for $C = 4$. (b) $\overline{\Delta L_p}$ (dB) as a function of the grid stretching and the grid resolution. Circles correspond to the theoretical minimum resolved wave number.

by $2\Delta_{max}/\Delta$, with $\Delta_{max} = \max(S_{\xi,max}, S_{\eta,max})\Delta = C\Delta$. The results indeed show values of $\overline{\Delta L_p}$ larger than $0\,dB$ for N_λ numbers smaller than indicated by the circles. For values of $C < 1$, the accuracy remains close to $N_\lambda = 2$. However, the stability and accuracy criterion for Δt should be respected as taking into account the various grid spacing.

B. Reflecting surface

1. Impedance plane

The accuracy of the locally reacting approach in the PSTD method is first demonstrated for a flat surface with a constant impedance, and a flat rigid surface with an impedance strip with width $w = 12\,\Delta$, see configurations (B1) and (B2) in Fig. 2. Three impedance values have been taken, as printed in Fig. 2, and represent a rigid ground surface or a ground surface with an absorption coefficient for normal incident sound waves of 0.2 and 0.8, respectively. For this configuration, no curvilinear approach needs to be taken, implying that the accuracy of the impedance approach is shown separate from the curvilinear approximation. Calculations are initiated with the conditions from Eq. (18). For the three impedance values, results are shown in Fig. 4 for $\Delta L_{p,n} = |L_{p,n} - L_{p,ref}|$, with $L_{p,ref}$ the reference result computed with an analytical solution according to Ref. 20 for configuration (B1) and with the boundary element method utilizing the openBEM toolbox[21] for configuration

(B2). In the boundary element method, at least 10 elements per wavelength have been used for all calculations. The results are shown as a function of the receiver angle θ and the N_λ number. The rigid ground case performs best and PSTD gives largest deviations for the softest ground (strip). The error increases with frequency and for angles close to grazing incidence. The results show that the finite strip width does not introduce additional errors compared to the surface with the constant impedance value. The results show that PSTD is most useful to represent locally reacting boundary surface with a high surface impedance. It can be noticed that the Fourier PSTD method has a high accuracy for extendedly reacting boundaries for real-valued surface impedances,[16] but this approach does not fit into the current framework of the curvilinear Fourier PSTD method as already pointed out.

2. Trapezoidal and Gaussian shaped impedance strip

For investigating the accuracy of the curvilinear Fourier PSTD method, configurations (B3) and (B4) from Fig. 2 are now considered. As for the flat ground surface, three values of the normalized surface impedance of the trapezoidal and Gaussian shaped strip with width $w = 12\,\Delta$ have been used. The same source and receiver positions have been adopted as in configurations (B1) and (B2). Calculations have been carried out for various heights of the trapezoid and Gaussian shape, i.e., H in Eq. (14) ranges
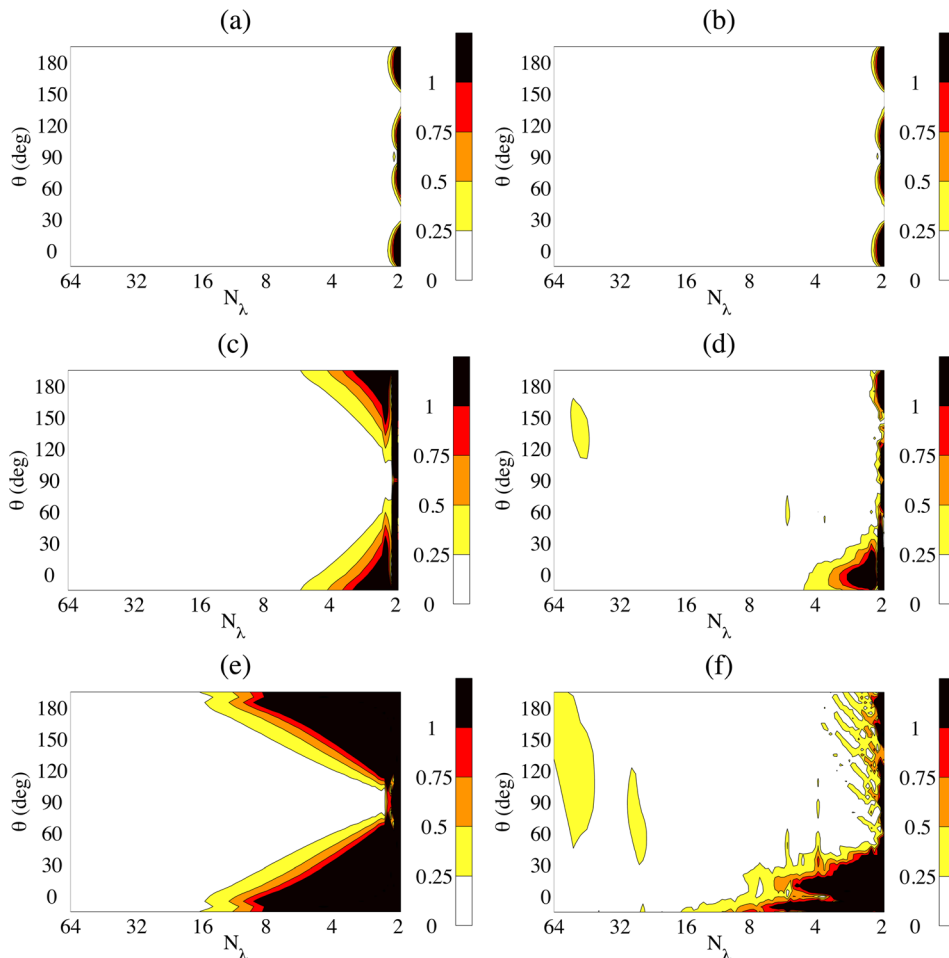

FIG. 4. (Color online) Results for configuration (left), (B1) and (right) (B2). $\Delta L_{p,n}$ (dB) as a function of the receiver position and N_λ for [(a), (b)] $Z_n = \infty$, [(c), (d)] $Z_n = 17.9$, [(e), (f)] $Z_n = 2.6$.
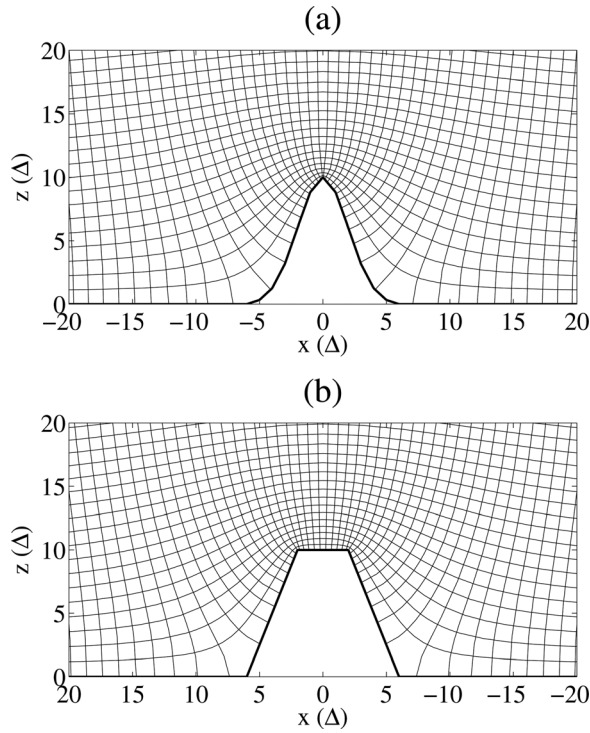
FIG. 5. Mesh close-up around a (a) Gaussian shape and (b) trapezoid, with (thick) modelled geometry (thin) u_η-mesh.

from 0 to 10Δ, and for two discretizations Δ and $\Delta' = \Delta/2$. For the discretization of Δ, $\overline{\Delta L_p}$ is plotted in Fig. 5 as a function of the N_λ number and H. As for configuration (B2), the boundary element method has been used to produce the reference results. For all three impedance values, a clear decrease of the accuracy is visible for an increasing height of the trapezoid. The error from the curvilinear PSTD method can be attributed to three causes. The first is the lower accuracy for the lower value of the surface impedance, as shown for configuration (B2). The second is the local stretching in the physical domain. Figure 5 indeed shows that the cells are locally larger near the Gaussian shape and trapezoid. To estimate the error from this stretching, the largest grid spacing is computed from the grids, and the corresponding smallest resolved wavelength is derived. These values will not fully explain $\overline{\Delta L_p}$ of Fig. 6, in contrast to the free field configuration (A). The third error is namely due to the approximation of modeling the boundary shape, and may be related to the maximum angular change of the surface shape that a grid cell needs to handle. To account for the latter two effects, the minimum N_λ number in all numerical calculations expressed by $N_{\lambda,\text{num}}$, for highest two impedance values, is fitted to the next model, the apparent resolved number of points per wavelength expressed by $N_{\lambda,\text{app}}$,
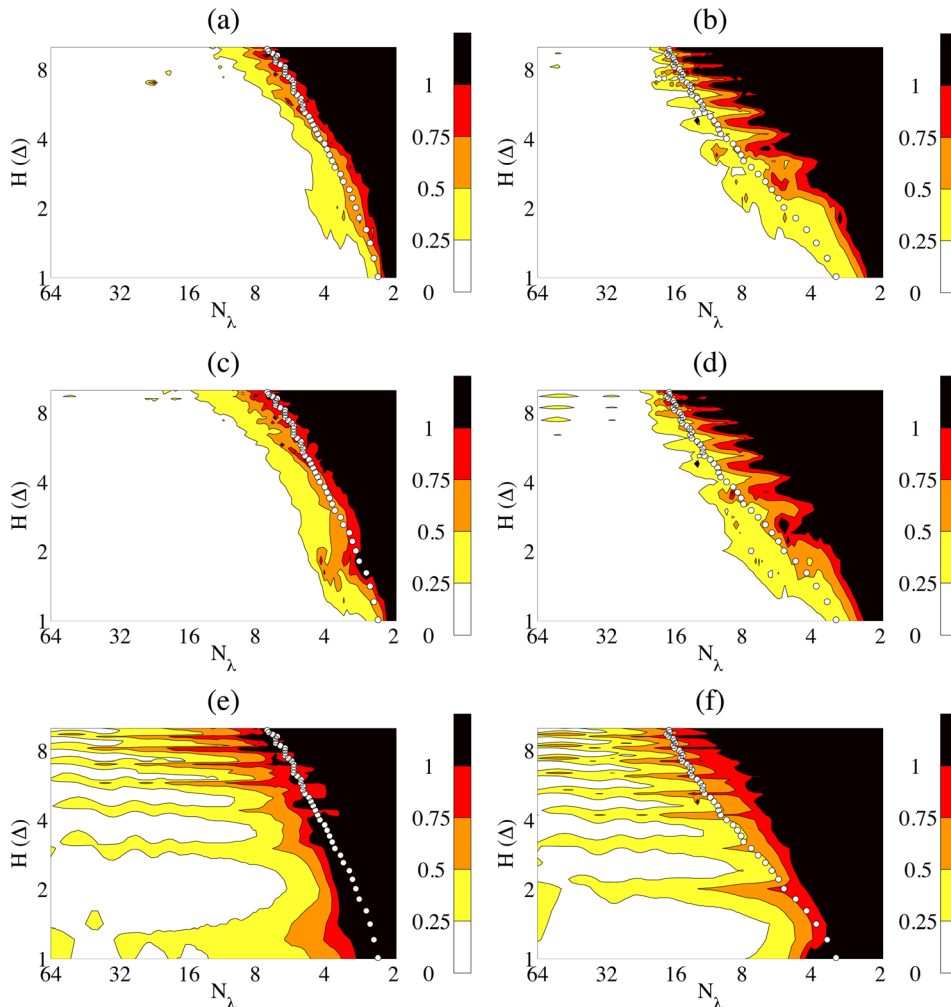

FIG. 6. (Color online) Results for configuration left, (B3) and right, (B4). $\overline{\Delta L_p}$ results for grid spacing Δ as a function of the Gaussian shape or trapezoid height H and N_λ for [(a), (b)] $Z_n = \infty$, [(c), (d)] $Z_n = 17.9$, [(e), (f)] $Z_n = 2.6$.
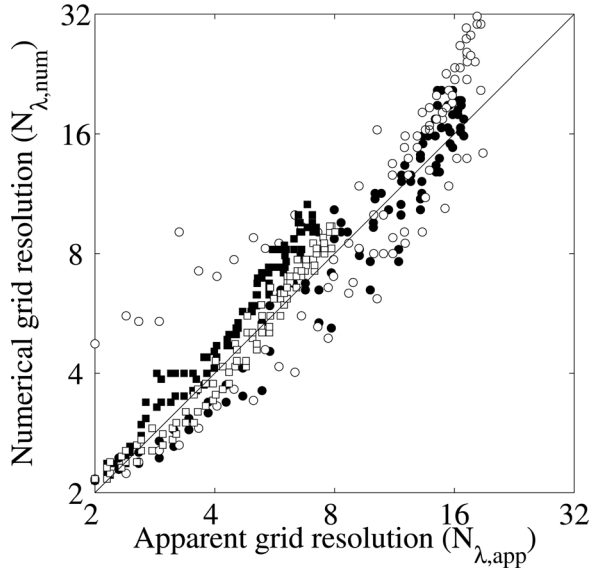
Maarten Hornikx and Didier Dragna

FIG. 7. Numerical point per wavelength requirement $N_{\lambda,\text{num}}$ versus modeled $N_{\lambda,\text{app}}$ number according to Eq. (19). Results from all calculations of configurations (B3) and (B4) for $Z_n = \infty$ and $Z_n = 17.9$. (Black circles) Trapezoid results, grid spacing Δ, (white circles) Trapezoid results, grid spacing $\Delta' = \Delta/2$, (black squares) Gaussian shape results, grid spacing Δ, (white squares) Gaussian shape results, grid spacing $\Delta' = \Delta/2$.

$$N_{\lambda,\text{app}} = \frac{2\Delta_{\text{max}}}{\Delta} + \kappa(\Delta\theta_{\text{max}})^\beta, \qquad (19)$$

with $\Delta\theta_{\text{max}}$ the maximum angular change of the boundary in the configuration and $\kappa = 1.1\,e^{-2}$ and $\beta = 1.64$ coefficients found from fitting to the computed $N_{\lambda,\text{num}}$, which is determined to be the N_λ value above which $\overline{\Delta L_p} > 0.5$ dB. The values of $N_{\lambda,\text{app}}$ are also shown by the circles in Fig. 6, indicating that a rather good prediction can be made from this model for the studied configurations. In Fig. 7, the numerical computed $N_{\lambda,\text{num}}$ values for all computed configurations are plotted against $N_{\lambda,\text{app}}$. The performance of the curvilinear PSTD for the configurations (B3) and (B4) from Fig. 2 is also compared with results from the staircase PSTD method, as shown in Fig. 8. This means that Eqs. (2) are directly solved by the PSTD method with Cartesian mesh. In the staircase PSTD method, boundary interfaces are located at acoustic velocity components, where the nearest velocity components to the shape of the trapezoid or Gaussian shape are taken as boundary interface. The staircase PSTD method performs worse than the curvilinear PSTD method, especially for the highest two impedance values and lower heights of the trapezoid and Gaussian shape. To emphasize the accuracy of the curvilinear Fourier PSTD method for $N_\lambda > N_{\lambda,\text{app}}$, Fig. 9 shows the excess attenuation $EA = L_p - L_{p,\text{free}}$ from the boundary element method as well as the curvilinear Fourier PSTD method for the configurations (B2), (B3), and (B4) as a function of the receiver position for $N_\lambda = 8$. The plot also shows the impact of the changed
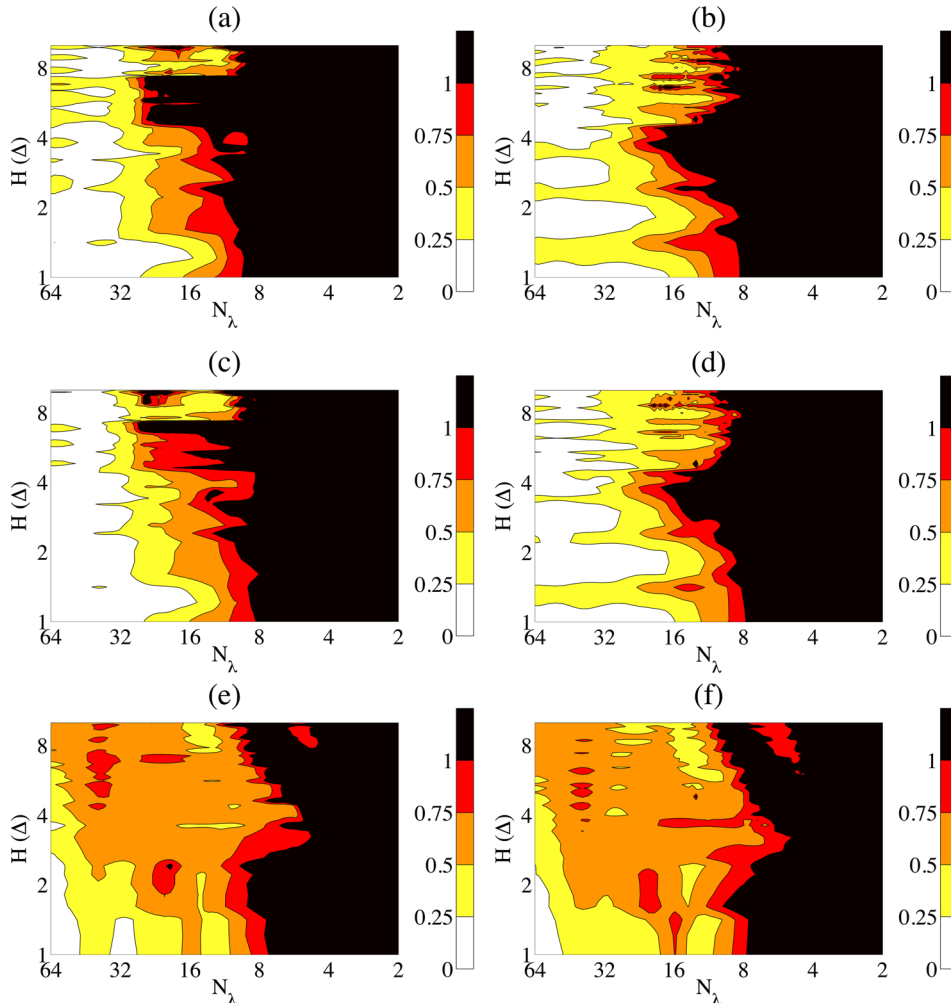

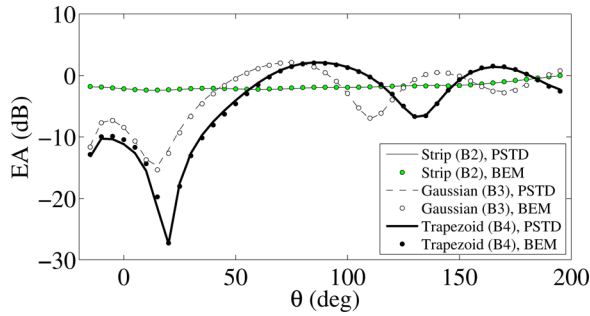FIG. 8. (Color online) As Fig. 6 but computed with the staircase PSTD method.

FIG. 9. (Color online) Excess attenuation for the three configurations (B) with $Z_n = 17.9$ as a function of the receiver position for $f = c/8\Delta$. Heights of the Gaussian shape and the trapezoid is 3Δ.

configuration, as the location of the interferences in the spectrum depends strongly on the ground profile. This is also visible from Fig. 10, where the computed impulse responses with the curvilinear Fourier PSTD method at receiver position $\theta = 90°$ are shown. The first arrival around $t = 200\Delta t$ is the direct wave and is the same for the three configuration as it does not depend on the boundary conditions. The second arrival around $t = 300\Delta t$, corresponding to the wave reflected/diffracted by the ground, is however seen to be modified by the ground profile. Furthermore, a third arrival can be distinguished around $t = 500\Delta t$ for the configuration (B4).

C. Inhomogeneous atmosphere

To demonstrate the applicability of the curvilinear Fourier PSTD method, sound propagation over a hill in an NBL is computed. In the configuration of Fig. 2(C), the direction of the wind velocity is from the source to the receiver positions. Since the temperature increases with height, temperature and wind velocity cause the sound waves to be bent downwards from source to receiver. Figure 11(a) shows the level difference $\Delta L_{p, n} = L_{p, n, \text{NBL}} - L_{p, n}$, with $L_{p, n, \text{NBL}}$ the level at the receiver positions in the presence of the nocturnal boundary layer and $L_{p,n}$ the levels for an atmosphere with a constant speed of sound of 340 m/s. The results are shown in 1/3 octave bands up to the band for which this computation is valid according to Eq. (19), which is the 1250 Hz 1/3 octave band with $\Delta = 0.1$ m, and $N_{\lambda, \text{app}} = 2.6$. Clearly, the large influence of the NBL is visible, with increased levels for the lower and higher frequencies, and
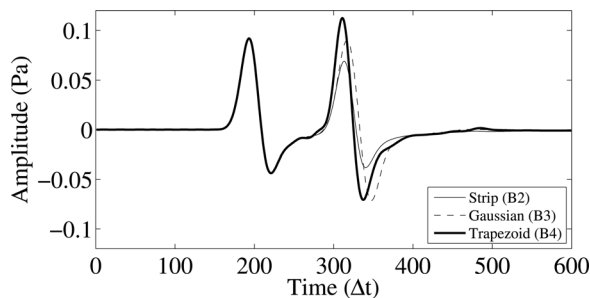

FIG. 10. Computed impulse responses with PSTD at receiver position with $\theta = 90$ degree, for the three configurations (B) with $Z_n = 17.9$.
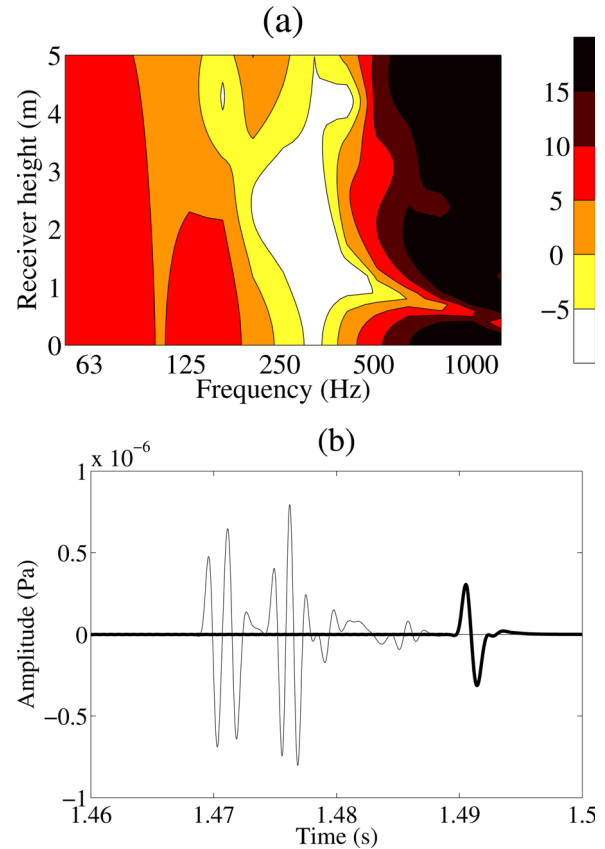

FIG. 11. (Color online) Results for configuration (C). (a) Excess level $\Delta L_{p,n}$ due to the nocturnal boundary layer (NBL) as a function of 1/3 octave band and receiver height, (b) computed impulse responses at receiver position (500 and 0 m). Results are calculated for sound propagation in an homogeneous atmosphere and in a NBL (thick and thin line, respectively).

lower levels around the 315 Hz 1/3 octave band. Figure 11(b) shows the computed impulse response at the receiver position at the ground, illustrating the earlier time of arrival in the presence of the NBL, as well as the longer response due to multiple reflections of the sound waves with the ground surface.

V. CONCLUSIONS

To compute atmospheric sound propagation in the presence of non-staircase type boundaries with the Fourier PSTD method, an efficient time-domain wave-based prediction method, a curvilinear approach has been taken for 2D configurations with real valued impedance boundary conditions. In free field, results show that a higher demand on discretization is needed as the grid gets more stretched. For configurations involving boundaries, an orthogonal curvilinear map is applied, yielding the advantage of applicability of computing pressure derivatives and velocity components normal to the boundaries as in the staircase PSTD method. Results have been compared with calculations using the boundary element method. The curvilinear Fourier PSTD method requires a higher number of discrete spatial grid points to resolve a single wavelength, i.e., higher than the two points per wavelength criterion of the Cartesian equidistant PSTD method and this number is shown to be related to the largest grid

Maarten Hornikx and Didier Dragna

spacing and the deformation of the boundary shape expressed in a maximum angular value. This approach is valid for boundaries with a high surface impedance, for which the used locally reacting approach is more applicable than for surfaces with low impedance values. The Fourier PSTD method has a lower accuracy for low-valued surface impedances. The applicability of the curvilinear Fourier PSTD method to compute outdoor sound propagation in the presence of a hill in a nocturnal boundary layer is finally demonstrated. The higher number of discrete points per wavelength, as well as the decreased discrete time step related to the smallest grid cell in the physical domain reduce the efficiency of the Fourier PSTD method for severe grid deformations. Therefore, from the investigated configurations, it may be concluded that the current curvilinear PSTD approach holds for problems with low grid deformations and boundaries with high surface impedances. The curvilinear PSTD method has shown to clearly outperform the staircase PSTD method for these cases. An extension to 3D configuration in which the third dimension may be modeled by a Cartesian mesh is straightforward. Further work also includes the application of the curvilinear method to the Fourier Continuation PSTD method where the geometry is divided into subdomains. Such a methodology does not require an orthogonal mapping as boundaries can be modeled by imposing boundary conditions. This increases the efficiency as the grid stretching values of S will remain modest. Also the combination of the curvilinear method with more advanced boundary conditions, i.e., boundary conditions with arbitrary impedance values, will be addressed.

ACKNOWLEDGMENTS

[1]T. Oshima, T. Ishizuka, and T. Kamijo, "Three-dimensional urban acoustic simulations and scale-model measurements over real-life topography," J. Acoust. Soc. Am. **135**, EL324–EL330 (2014).

[2]R. Cheng, P. J. Morris, and K. S. Brentner, "A three dimensional parabolic equation method for sound propagation in moving inhomogeneous media," J. Acoust. Soc. Am. **126**, 1700–1710 (2009).

[3]G. Guillaume, J. Picaut, G. Dutilleux, and B. Gauvreau, "Time-domain impedance formulation for transmission line matrix modelling of outdoor sound propagation," J. Sound. Vib. **330**, 6467–6481 (2011).

[4]M. Hornikx, R. Waxler, and J. Forssén, "The extended Fourier pseudospectral time-domain method for atmospheric sound propagation," J. Acoust. Soc. Am. **128**, 1632–1646 (2010).

[5]M. Hornikx, W. De Roeck, and W. Desmet, "A multi-domain Fourier pseudospectral time-domain method for the linearized Euler equations," J. Comp. Phys. **231**, 4759–4774 (2012).

[6]N. Albin, O. P. Bruno, T. Y. Cheung, and R. O. Cleveland, "Fourier continuation methods for high-fidelity simulation of nonlinear acoustic beams," J. Acoust. Soc. Am. **132**, 2371–2387 (2012).

[7]J. B. Schneider, C. L. Wagner, and R. J. Kruhlak, "Simple conformal methods for finite-difference time-domain modeling of pressure-release surfaces," J. Acoust. Soc. Am. **104**, 3219–3226 (1998).

[8]O. Marsden, C. Bogey, and C. Bailly, "High-order curvilinear simulations of flows around non-Cartesian bodies," J. Comp. Acoust. **13**, 731–748 (2005).

[9]D. Dragna, P. Blanc-Benon, and F. Poisson, "Time-domain solver in curvilinear coordinates for outdoor sound propagation over complex terrain," J. Acoust. Soc. Am. **133**, 3751–3763 (2013).

[10]Y. Q. Zeng, Q. H. Liu, and G. Zhao, "Multidomain pseudospectral time-domain (PSTD) method for acoustic waves in lossy media," J. Comp. Acoust. **12**, 277–299 (2004).

[11]S. Bilbao, "Modeling of complex geometries and boundary conditions in finite difference/finite volume time domain room acoustics simulation," IEEE Trans. Audio, Speech, Lang. Process. **21**, 1524–1533 (2013).

[12]J. Häggblad and B. Engquist, "Consistent modeling of boundaries in acoustic finite-difference time-domain simulations," J. Acoust. Soc. Am. **132**, 1303–1310 (2012).

[13]P. Nielsen, F. If, P. Berg, and O. Skovgaard, "Using the pseudospectral technique on curved grids for 2D acoustic forward modelling," Geophys. Prospect. **42**, 321–341 (1994).

[14]R. Waxler, C. L. Talmadge, S. Dravida, and K. E. Gilbert, "The near-ground structure of the nocturnal sound field," J. Acoust. Soc. Am. **119**, 86–95 (2006).

[15]C. Bogey and C. Bailly, "A family of low dispersive and low dissipative explicit schemes for flow and noise computation," J. Comp. Phys. **194**, 194–214 (2004).

[16]M. Hornikx and R. Waxler, "The extended Fourier pseudospectral time-domain (PSTD) method for fluid media with discontinuous properties," J. Comp. Acoust. **18**, 297–319 (2010).

[17]T. A. Driscoll, "A MATLAB toolbox for Schwarz-Christoffel mapping," ACM Trans. Math. Software **22**, 168–186 (1996).

[18]T. A. Driscoll, "Improvements to the Schwarz-Christoffel toolbox for MATLAB," ACM Trans. Math. Software **31**, 239–251 (2005).

[19]L. Mahrt, "Surface heterogeneity and vertical structure of the boundary layer," Boundary-Layer Meteorol. **96**, 33–62 (2000).

[20]S. N. Chandler-Wilde and D. C. Hothersall, "Efficient calculation of the Green's function for acoustic propagation above a homogeneous impedance plane," J. Sound Vib. **180**, 705–724 (1995).

[21]V. Cutanda Henriquez and P. M. Juhl, "OpenBEM—An open source Boundary Element Method software in Acoustics," in *Proceedings of Internoise*, Lisbon, Portugal (2010).